Journal of the European Ceramic Society 22 (2002) 2123–2132

www.elsevier.com/locate/jeurceramsoc

Pyroelectric properties of Mn-doped lead zirconate–lead titanate–lead magnesium niobate ceramics

C.P. Shaw*, S. Gupta[1], S.B. Stringfellow, A. Navarro, J.R. Alcock, R.W. Whatmore

Nanotechnology, S.I.M.S, Cranfield University, Cranfield, Bedfordshire, UK

Received 15 September 2001; accepted 29 December 2001

Abstract

The pyroelectric properties of MnO_2 doped compositions in the $Pb(Mg_{1/3}Nb_{2/3})O_3$–$PbTiO_3$–$PbZrO_3$ system have been investigated for an uncooled pyroelectric infrared detecting application, looking primarily at compositions in the $PbZrO_3$-rich corner of the phase diagram. A processing route from the metal oxides through to the poled ceramic has been developed, which has reduced the size and frequency of defects in the sintered ceramic necessary for producing thin (~200 μm) ceramic wafers. The electrical properties relevant to the pyroelectric application (dielectric constant, tanδ and pyroelectric coefficient) have been surveyed with respect to composition to produce the best values of the pyroelectric 'figure of merit' $F_D = p/\{c'(\varepsilon\varepsilon_o\tan\delta)^{1/2}\}$ at room temperature. The effects of compositional changes in the ceramic on the two phase transitions from: the ferroelectric low temperature to ferroelectric high temperature phases ($F_{R(LT)}$ to $F_{R(HT)}$) and the ferroelectric high temperature to paraelectric phases at the Curie point have also been investigated. The consequential changes of the electrical properties are reported. The resisitivity of the ceramic proved insensitive to either the amounts of excess lead or manganese doping levels.

Keywords: Doping; PMN-PZT; Processing; Pyroelectric properties; Electrical resistivity

1. Introduction

The use of ferroelectric oxide ceramics in uncooled pyroelectric infrared detection and thermal imaging applications has been studied for a number of years.[1] The electrical properties of such materials for different pyroelectric applications can be optimized through the use of pyroelectric "figures of merit" (FOM).[1–5] These are combinations of the electrical properties of the pyroelectric material that are directly related to the performances of the devices for these applications. The most commonly used FOMs are:

$$F_i = p/c \tag{1}$$

where the current responsivity of the device is proportional to F_i

$$F_v = p/(c'\varepsilon_o\varepsilon) \tag{2}$$

where the voltage responsivity of the device is proportional to F_v

$$F_D = p/\left(c(\varepsilon_o\varepsilon\tan\delta)^{0.5}\right) \tag{3}$$

where the specific detectivity of the device is proportional to F_D.

In these formulae:

p	=	pyroelectric coefficient
c'	=	volume specific heat
ε	=	dielectric permittivity at the frequency of device operation
$\tan\delta$	=	dielectric loss tangent at the frequency of device operation
ε_o	=	dielectric permittivity of free space

In an ideally matched voltage-mode pyroelectric device the input capacitance of the voltage amplifier linked to the pyroelectric element would be similar in magnitude to that of the element itself. In this case, the FOM F_D is the most relevant. In devices where the element capacitance is much larger than the amplifier capacitance, or where the AC Johnson Noise in the ele-

* Corresponding author.
E-mail address: c.p.shaw@cranfield.ac.uk (C.P. Shaw).
[1] Laser Materials Division, Centre for Advanced Technology, Indore -452013, India.

0955-2219/02/$ - see front matter
PII: S0955-2219(02)00018-3

ment does not dominate in the noise figure for the device, F_V is appropriate. F_i is most appropriate when the element capacitance is much smaller than the amplifier capacitance.

Although the FOM values are important indicators of material suitability, a number of other properties have to be addressed for workable devices. Working temperature range, physical stability and material availability (cost/volume) are all important considerations. The devices need to operate over a wide range of ambient temperatures (say −40 to +70 °C), ideally without temperature control, which is one advantage they hold over cooled photoconductive detectors. Various single crystal materials based on triglycine sulphate (TGS) possess high FOM but suffer from low Curie temperatures, water solubility and poor handling characteristics. Thin single crystal sections of materials such as lithium niobate and lithium tantalate, which are produced by lapping and polishing, tend to be fragile. The presence of phase changes in or near the working temperature window can also produce undesirable non-linear pyroelectric responses on heating and cooling.

Pyroelectric polycrystalline oxide ceramics such as those based on lead titanate—PT[6,7] or lead zirconate titanate—PZT[8–10] offer a number of improvements over single crystal materials. They are robust materials, which are chemically inert. Their good strength allows large area wafers to be made, which can then be easily machined into thin sections. The wide variety of solid solution systems that can be made with these ceramics allows control of the electrical properties over large ranges.

A number of studies into different solid solutions of PZT and PT with other ceramic oxides have been reported for pyroelectric applications. In the undoped $PbZr_{(1-y)}Ti_yO_3$ system, two phase changes are observed at 255 and 70 °C when $y=0.1$. The upper transition is the Curie point [paraelectric to high temperature ferroelectric rhombohedral ($F_{R(HT)}$) phase transition] whereas the lower is the high temperature ferroelectric rhombohedral ($F_{R(HT)}$) to low temperature ferroelectric rhombohedral ($F_{R(LT)}$) phase transition. The possibility of using the large pyroelectric coefficient associated with this lower transition, and the ability to shift the transition temperature with suitable doping has been a major area of investigation. Examples of this have been bismuth doped PZT,[11] PZT in solid solution with Pb_2FeNbO_3,[8] and undoped PZT.[12] Particular issues with this mode of use are the thermal hysteresis which occurs in the $F_{R(LT)} \rightarrow F_{R(HT)}$ phase transition because of its first-order nature[11] and the fact that its use would entail some form of device thermal stabilisation. The latter issue need not be a major problem, if the consequent performance increase is great enough, as has been seen with the use of so-called dielectric bolometer mode materials such as lead scandium tantalate.[13]

There has been no work reported to date on the pyroelectric properties of rhombohedral compositions of PZT in solid solution with lead magnesium niobate (PMN). Previous studies[14–16] have focussed on the piezoelectric properties of compositions in the system, mainly in the region of the morphotropic phase boundary, or on the pyroelectric properties of tetragonal compositions close to PT.[18] Ouchi et al.[14] reported the piezoelectric and dielectric properties of the $Pb(Mg_{1/3}Nb_{2/3})O_3$–$PbTiO_3$–$PbZrO_3$ system, covering most of the phase diagram.

This study has been useful in that it points to regions of the phase diagram where the dielectric constants of compositions are relatively low (<300) and it also documented synthesis and sintering conditions. Further studies[15,16] where the effects of different additives were explored showed that MnO_2 additions significantly reduced both the dielectric constant and loss values.

This work reports the pyroelectric properties of MnO_2 doped compositions in the $Pb(Mg_{1/3}Nb_{2/3})O_3$–$PbTiO_3$–$PbZrO_3$ system, looking primarily at the $PbZrO_3$-rich corner of the phase diagram.[26] Two major goals have been optimisation of the electrical parameters (dielectric constant, tanδ and pyroelectric coefficient) to produce high FOMs, and a study of how these properties change in the region of the $F_{R(LT)}$ to $F_{R(HT)}$ phase transition.

2. Experimental

A mixed oxide route was used to prepare different batches of ceramic material based on the general formula: $Pb_{1+\delta}[(Zr_{1-x}Ti_x)_{1-y}(Mg_{1/3}Nb_{2/3})_y]_{1-z}Mn_zO_3$. For this paper, this formula has been given the acronym PZTMNM. The coded abbreviation P[[1 + δ].100]ZTMNM[x.100]/[y.100]/[z.100] is used to denote a particular composition which are summarised in Table 1. Lead (II) oxide (BDH, GPR), titanium (IV) oxide (Aldrich, −325 mesh), zirconium (IV) oxide (Aldrich, <5 μm), manganese (IV) oxide (BDH, GPR) and magnesium niobate[19] were the reagents used in the main ceramic synthesis. The magnesium niobate was prepared from basic magnesium carbonate [$Mg(CO_3)\cdot Mg(OH)_2\cdot 5H_2O$] (Aldrich) and niobium (V) oxide (Aldrich, −325 mesh) in an initial step using the route described by Butcher and Daglish.[20]

Fig. 1a shows the schematic experimental route followed to produce calcined powders of the magnesium niobate and the PZTMNM batches. In the milling stages, powders were dispersed in 0.1 wt.% aqueous dispex A40 (Allied Colloids) solution and milled in polyethylene pots with yttrium-stabilised zirconia pellets. Drying was carried out in a fan-assisted oven at 65 °C for 24 h, whilst sieving (Endecotts™ steel mesh) was facilitated using a combination of mortar and pestle, and a nylon brush. The powders were calcined in a

Table 1
Composition coding table in terms of atomic fractions[a]

Composition No.	Code	$d\times100$ PbO Xs	$x\times100$ At.% Ti	$y\times100$ At.% MgNb	$z\times100$ At.% Mn
1	P101ZTMNM2.5/2.5/1	1.00	2.50	2.50	1.00
2	P101ZTMNM7.5/2.5/1	1.00	7.50	2.50	1.00
3	P101ZTMNM12.5/2.5/1	1.00	12.50	2.50	1.00
4	P101ZTMNM17.5/2.5/1	1.00	17.50	2.50	1.00
5	P101ZTMNM2.5/7.5/1	1.00	2.50	7.50	1.00
6	P101ZTMNM7.5/7.5/1	1.00	7.50	7.50	1.00
7	P101ZTMNM12.5/7.5/1	1.00	12.50	7.50	1.00
8	P101ZTMNM2.5/12.5/1	1.00	2.50	12.50	1.00
9	P101ZTMNM7.5/12.5/1	1.00	7.50	12.50	1.00
10	P101ZTMNM12.5/12.5/1	1.00	12.50	12.50	1.00
11	P101ZTMNM7.5/17.5/1	1.00	7.50	17.50	1.00
12	P101ZTMNM7.5/7.5/0.5	1.00	7.50	7.50	0.50
13	P101ZTMNM7.5/7.5/1.2	1.00	7.50	7.50	1.20
14	P101ZTMNM7.5/7.5/1.5	1.00	7.50	7.50	1.50
15	P101.5ZTMNM17.5/2.5/1	1.50	17.50	2.50	1.00
16	P102ZTMNM17.5/2.5/1	2.00	17.50	2.50	1.00

[a] For d, x, y, z in the formula $Pb_{1+d}\{[(Zr_{1-x}Ti_x)_{1-y}(Mg_{1/3}N_{2/3})_y]_{1-z}Mn_z\}O_3$.

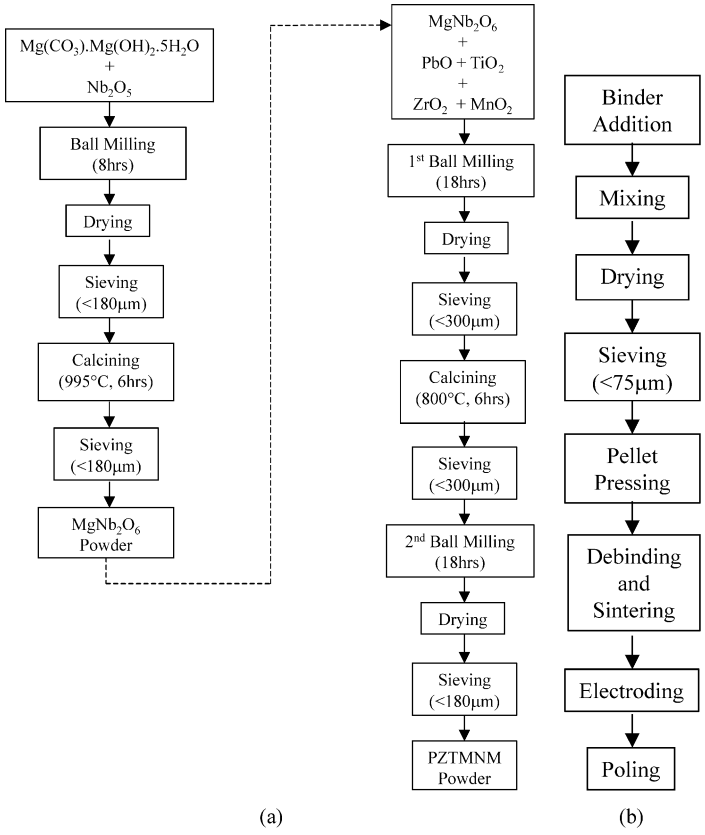

Fig. 1. (a) Processing route for $MgNb_2O_6$ and PZTMNM powder preparation; (b) processing route to produce poled sintered samples.

covered alumina crucible in a muffle furnace with an air atmosphere. X-ray diffraction (XRD) studies were made to determine the best calcination temperatures. A Philips PW1720 diffractometer was used with iron filtered cobalt K_α radiation (wavelength 1.789 Å, slit width 0.05 mm).

Fig. 1b shows the route followed to consolidate the calcined PZTMNM powders into bulk ceramic pellets. Aqueous binder solutions of Glascol® (Allied Colloids) or 40/60 wt./wt. polyvinyl alcohol (PVA)/polyethylene glycol (PEG) were mixed with the PZTMNM powders using a variety of manual, ultrasonic and high shear

(Silverson™) mixing. The powder loading in the slurries was between 25 and 30% by volume, and the binder content in the dried, bound powder was varied between 1 and 4% by volume. Pellets were pressed using a 30 mm diameter, tapered punch and die set in a floating die arrangement, which was lubricated with stearic acid. The pellets were prestressed at 42 MPa and then loaded at 126 MPa for 2 min before expulsion.

Pellets were placed uncovered on an alumina tray for the debinding process, which included 2 h dwell times at 250 and 600 °C. For the sintering process, the pellets were stacked and separated with platinum sheets on a lapped alumina tray. The stack was covered with an alumina crucible whose rim had also been lapped to form a good seal with the tray, to help prevent lead loss at the elevated sintering temperatures. Sintering was carried out at 1250 and 1300 °C for 45 min with a 3 °C/min heating and 2 °C/min cooling ramp profile.

For the electrical characterisation, the pellets were electroded using silver paste, which was fired at 850 °C for 5 min in the muffle furnace. Samples were poled under an electric field of 3 kV/mm in hot mineral oil at 120 °C for 10 min. The field was supplied from a Keithley high voltage source, which was maintained until the oil temperature had cooled to <45 °C. The samples were then placed in an oven at 50 °C for 12 h with their electrodes shorted, to remove any space charges that might have been introduced by the poling process. The dielectric properties of the electroded pellets were measured using a GenRad 1689M RLC Digibridge. It should be noted that most pyroelectric devices are used at low frequencies (<100 Hz). Hence the dielectric properties reported here, and used to calculate the FOM are those measured at 33 Hz. The pyroelectric current response of each sample was measured using the Byer–Roundy method[21] on a custom-built computer controlled rig. This used a thermoelectric heater/cooler to ramp the specimen temperature within the range 20–90 °C, whilst under reduced pressure. The pyroelectric coefficients reported here are the averages of those measured on heating and on cooling. To determine the Curie temperature, dielectric properties of samples were measured over the range 20–300 °C, using a HP4092A Impedance Analyser. Ferroelectric hysteresis was measured at room temperature using a Radiant Technologies RT66A system operating in virtual ground mode.

3. Results

3.1. Ceramic processing

Fig. 2 shows the different PZTMNM compositions across the zirconia rich region of the ternary phase diagram in terms of the atomic fraction levels of, Ti, $Mg_{1/3}Nb_{2/3}$ and Zr, where all the compositions include 1 at.% excess of Pb and 1 at.% of Mn, based on the general formula previously mentioned. Figs. 3 and 4a show the XRD patterns with appropriate indexing of the peaks for the calcined powders from the initial magnesium niobate (calcined at 995 °C) and P101ZTMNM7.5/ 7.5/1 (composition 6) (calcined at 800 °C) synthesis steps. Both powders are single phase. Fig. 4b shows the XRD pattern from a sintered pellet of this composition after annealing at 1250 °C, and shows the development of the peaks caused by sintering. Green density measurements for the bound pellets fell in the range 57–61% of the theoretical density (8.0 g/cm^3 as determined from XRD) for the binder content and pressing pressures used.

The sintered pellets were black in colour and showed a 13 ± 1% decrease in both diameter and thickness from the green state. Archimedes densities measured after sintering were found to be ~97%. Optical studies of the surfaces of the pellets sintered at 1250 °C showed a relatively large grain size of 5–10 μm. This grain size

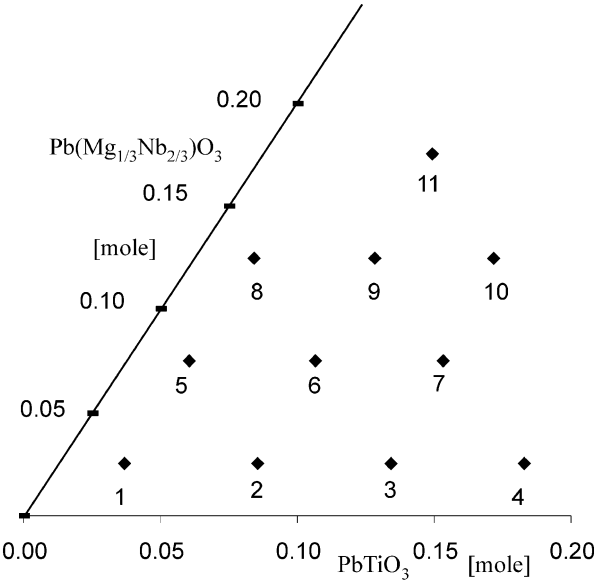

Fig. 2. Ternary phase diagram showing composition coding numbers for PZTMNM samples (compositions Nos. 1–11 contained 1 mol% excess PbO and 1 mol% MnO_2).

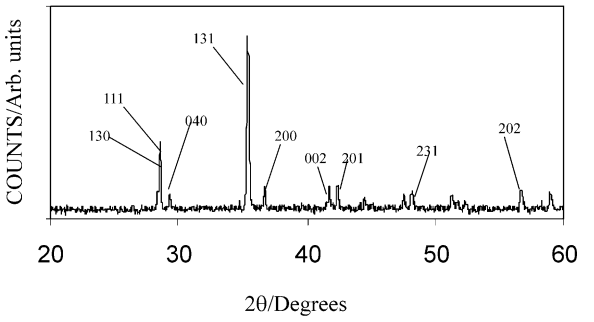

Fig. 3. XRD pattern of calcined product of $MgNb_2O_6$ powder synthesis step.

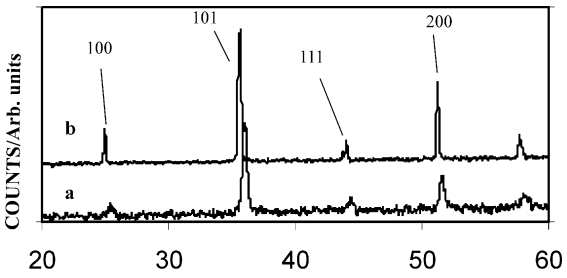

Fig. 4. XRD patterns of: (a) calcined product of PZTMNM (composition 6) powder synthesis step; (b) sintered pellet of composition 6.

was seen to increase to 10–20 μm when the sintering temperature was raised to 1300 °C. Optical microscopy and image analysis of the pellet surfaces after lapping and polishing helped to determine porosity and defect problems in the ceramic using optical techniques. The maximum defect size was found to be ~150 μm in samples pressed from bound powders which had been sieved only to <180 μm. This value was reduced to ~60 μm with a <75 μm sieve, although frequency of defects was still relatively high. Attempts to reduce the size and number of defects by decreasing the amount of binder used resulted in poorly pressed pellets, which tended to crack during debinding or sintering. A significant reduction in the number of defects was achieved by introducing a short heat treatment step (650 °C for 5 min) before the binder addition stage to remove polymeric particulate contaminants introduced from the milling pots. A full treatment of the use of experimental design to optimize pellet quality has been described elsewhere.[17] The results of the electrical measurements taken from these pellets as a function of composition are summarised in Figs. 5–13.

3.2. $F_{R(LT)} \rightarrow F_{R(HT)}$ and Curie point phase transitions

The determination of the $F_{R(LT)} \rightarrow F_{R(HT)}$ and Curie point phase transitions were obtained by observing anomalies in the plots of pyroelectric coefficients and dielectric properties with temperature. Fig. 5 shows the variation of pyroelectric coefficients as a function of temperature for three of the compositions (6, 7 and 9). For composition 6, it can be seen that the $F_{R(LT)} \rightarrow F_{R(HT)}$ phase transition is quite sharp at 65 °C on heating and shows about 9 °C of thermal hysteresis. The peak in the pyroelectric coefficient is very high, rising to a maximum of over 30×10^{-4} cm^{-2} K^{-1}. The transition is very sensitive to both PT and PMN content. Increasing the PT content to 12.5 mol%, while holding the PMN content constant at 7.5 mol% (composition 7), increases the $F_{R(LT)} \rightarrow F_{R(HT)}$ phase transition temperature to 96 °C. On the other hand, increasing the PMN content to 12.5 mol%, while holding the PT content constant at 7.5 mol% (composition 9), reduces the $F_{R(LT)} \rightarrow F_{R(HT)}$ phase transition temperature to 49 °C,

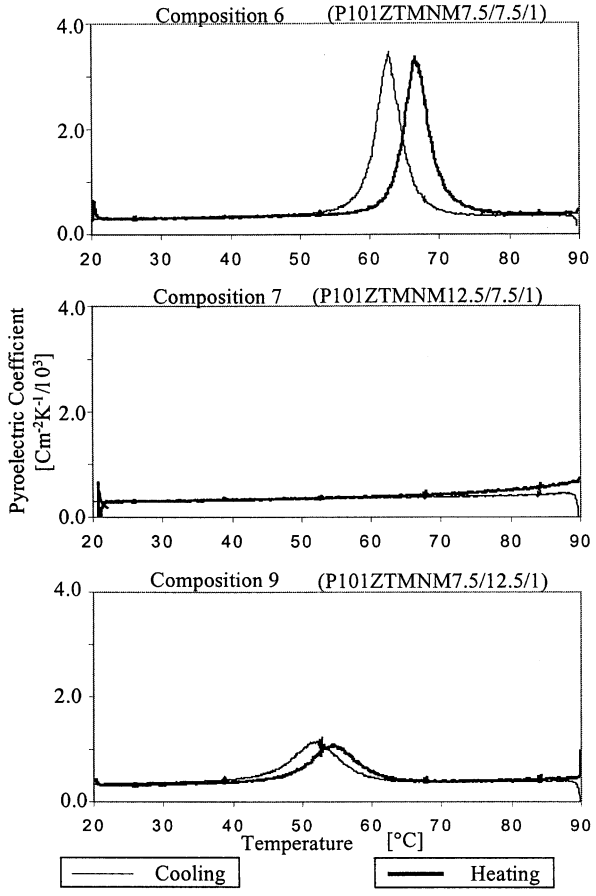

Fig. 5. Plots of pyroelectric coefficient vs. temperature for compositions 6, 7 and 9.

whilst also reducing the hysteresis to 5 °C. The transition is considerably more diffuse in composition 9 than composition 6, and the peak in the pyroelectric coefficient is reduced, to a maximum of around 12×10^{-4} cm^{-2} K^{-1}. In samples where the $F_{R(LT)} \rightarrow F_{R(HT)}$ phase transition temperature was outside the range covered by the pyroelectric rig a value was estimated from the anomaly in the dielectric constant versus temperature curve.

Fig. 6 shows the variation of dielectric properties with temperature for composition 6, which clearly shows the anomaly in both the dielectric loss and the dielectric constant (inset Fig. 6) curves, associated with the $F_{R(LT)} \rightarrow F_{R(HT)}$ phase transition. The $F_{R(LT)} \rightarrow F_{R(HT)}$ phase transition temperatures (heating and cooling) are plotted as a function of composition in Fig. 7, while the Curie temperatures (heating and cooling) are plotted in Fig. 8. It can be seen that there is a general tendency for both transitions to increase with increasing PT content and reduce with increasing PMN content.

3.3. Electrical properties vs. composition

Fig. 9 shows the variation with composition of the post-poling dielectric constant and loss at 33 Hz. It can

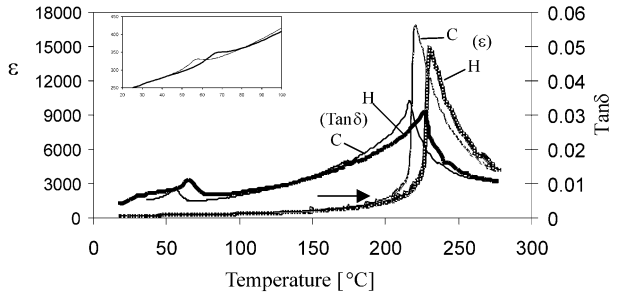

Fig. 6. Plot of dielectric properties (composition 6) vs. temperature showing Curie point. (Inset shows enlargement of ε vs temperature curve in the $F_{R(LT)} \rightarrow F_{R(HT)}$ phase transition region. H and C indicate heating and cooling cycles).

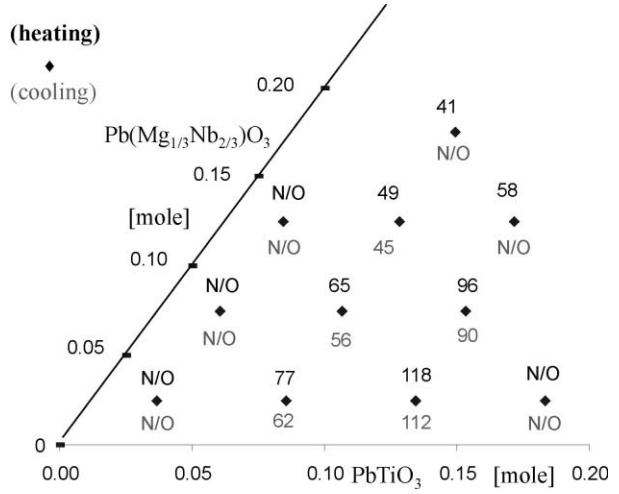

Fig. 7. Ternary diagram showing $F_{R(LT)} \rightarrow F_{R(HT)}$ phase transition temperatures determined from heating /cooling cycles of the dielectric constant vs. temperature plots (N/O indicates the transition was not observed.).

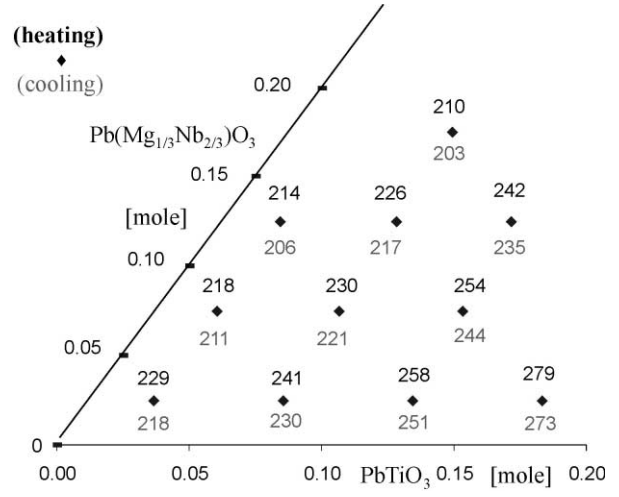

Fig. 8. Ternary diagram showing Curie point temperatures determined from peak maxima of dielectric constant vs. temperature plots for heating/cooling cycles.

be seen that there is a slight tendency for the dielectric constant to increase with increasing PMN content, with a marked increase for the highest PMN content (P101 ZTMNM7.5/17.5/1). This composition also exhibited by far the highest dielectric loss (0.026) at this frequency. The pyroelectric coefficients (measured at 30 °C) are plotted in Fig. 10 and the figures-of-merit F_V and F_D calculated from these and the 33 Hz dielectric data in Fig. 11. The resistivity of a pyroelectric ceramic is also an important consideration as (in the absence of a gate bias resistor on the FET amplifier[1–5]) it determines the electrical time constant and bias point of the device using it. Fig. 12a shows the variation with composition of electrical resistivity (measured at a few volts bias). In addition to the compositions shown in Fig. 2, Fig. 12b shows resistivity measurements made on a number of

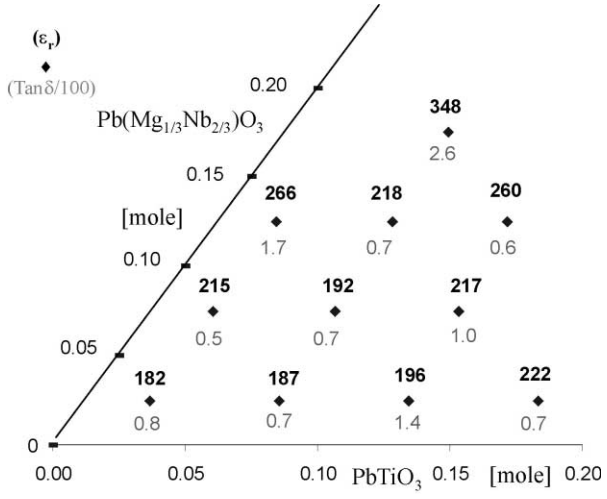

Fig. 9. Ternary diagram showing dielectric properties of PZTMNM compositions (measured at 33 Hz).

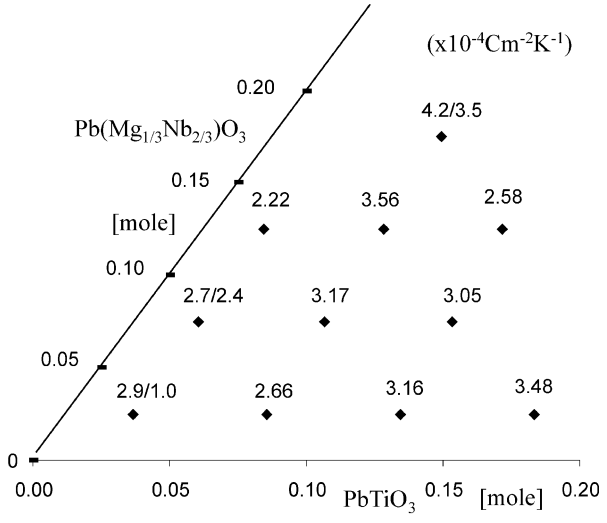

Fig. 10. Ternary diagram showing showing pyroelectric coefficients measured at 30 °C (heating/cooling values given where different).

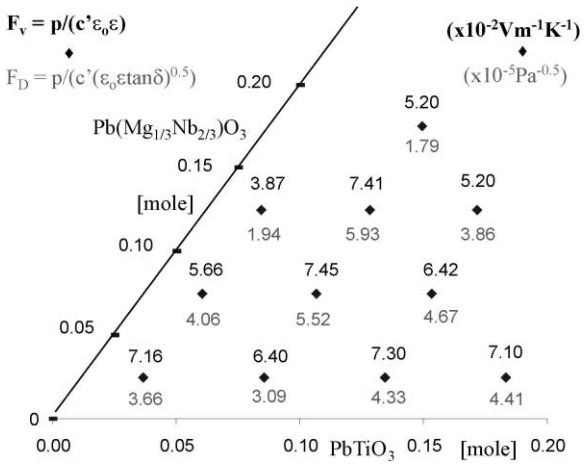

Fig. 11. Ternary diagram showing figure of merit values.

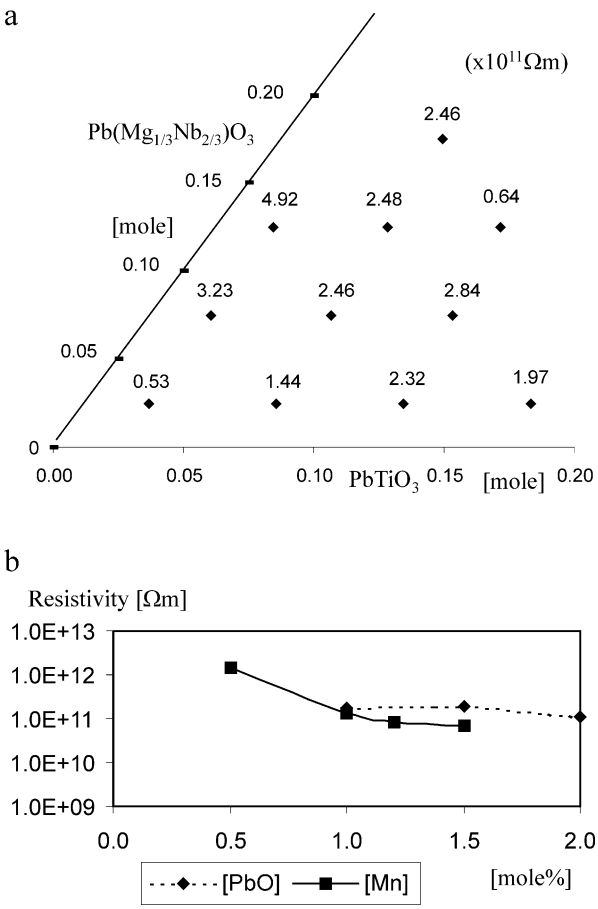

Fig. 12. Variation of resistivity with composition: (a) across ternary phase diagram; (b) as a function of PbO excess (based on composition 4) and manganese doping levels (based on composition 6).

other compositions in which the Pb excess, or the Mn content was varied.

4. Discussion

4.1. Ceramic processing

The XRD results for the calcined powders show that good agreement with the expected pattern for magnesium niobate and a rhombohedral material was achieved for the respective calcination temperatures and times. The XRD for the sintered pellet was also consistent with the rhombohedral perovskite pattern. The use of lapped alumina plates and crucible covers was successful in keeping sintering losses to <0.75 wt.%. The presence of pot debris from the final milling stage was believed to be responsible for the introduction of a large proportion of defects found in the early samples. The introduction of the heat treatment stage after the second milling was successful in removing any defects from polyethylene pot debris, sieve brush or included dust.

4.2. FOM and related dielectric and pyroelectric parameters

The investigation of the electrical properties of the PZTMNM samples showed a number of compositions whose FOM values (Fig. 11) compare favorably with commercial ceramics. Results from a modified lead titanate[8] and a modified lead zirconate,[27] report F_V values of 6×10^{-2} and 7×10^{-2} $Vm^2\ J^{-1}$, and F_D values of 5.8×10^{-5} and 3.2×10^{-5} $Pa^{-1/2}$, respectively. Fig. 11 clearly shows a number of compositions with either equivalent or better FOM values than these, so on purely the criteria of electrical properties these ceramic compositions offer viable pyroelectric material.

The zirconate rich region of the phase diagram had been chosen in this study as the previous work[14] had shown relatively low dielectric constants for similar compositions. Fig. 9 shows that post poling dielectric constants and losses were typically low and, as such, contributed to good FOM values. Fig. 9 also shows the general trend that the dielectric constant increased with increasing $Mg_{1/3}Nb_{2/3}$ and Ti concentrations. Fig. 5 shows the effect of the $F_{R(LT)}$ to $F_{R(HT)}$ phase transition on the pyroelectric coefficient for compositions 6, 7 and 9. The large hysteresis effect between heating and cooling is also apparent for compositions 6 and 9, whereas only the shoulder of the transition for composition 7 is observed because of the shift in transition temperature outside the range of the "Pyrorig". Comparison of the pyroelectric coefficients (at 30 °C) for these compositions from Fig. 10 shows that composition 9 has a significantly higher value than the other two compositions. However, Fig. 5 shows that the position of the $F_{R(LT)}$ to $F_{R(HT)}$ phase transition, which contributes to the increased pyroelectric coefficient below the upper operating temperature limit (70 °C) would rule composition 9 out as a commercial ceramic formula. In contrast,

composition 7 has no such problem from the phase transition and would offer a better choice as a commercial ceramic formula even with its diminished pyroelectric coefficient. Similarly, composition 20 showed a significantly higher dielectric constant compared to the other samples, due to the shifting of the $F_{R(LT)}$ to $F_{R(HT)}$ phase transition towards room temperature. The effect of this lowering in the transition temperature did however give the largest pyroelectric coefficient observed for all the samples. Fig. 7 summarises the observed positions of the $F_{R(LT)}$ to $F_{R(HT)}$ phase transition using a combination of data obtained from pyroelectric and dielectric vs. temperature plots. In a number of cases the phase transition was not observed because the transition was either too diffuse or may have been below room temperature.

4.3. Low Ti-compositions

It was interesting to note that composition 8 was anomalous in that the dielectric constant increased with poling. Compositions 1 and 5, which both contained the least Ti content (like composition 8) showed quite small reductions in dielectric constant and poor pyroelectric properties. This may be related to some antiferroelectric nature in these compositions, although the hysteresis results in Fig. 13 for compositions 5 and 8 do not show the characteristic double loop shape that might be expected for an antiferroelectric phase.

For the PZT phase diagram, it is well documented that an antiferroelectric phase exists for Ti content <6 mol%, and that an antiferroelectric–$F_{R(HT)}$ phase transition might be expected for compositions containing low amounts of Ti. It is worth noting that compositions

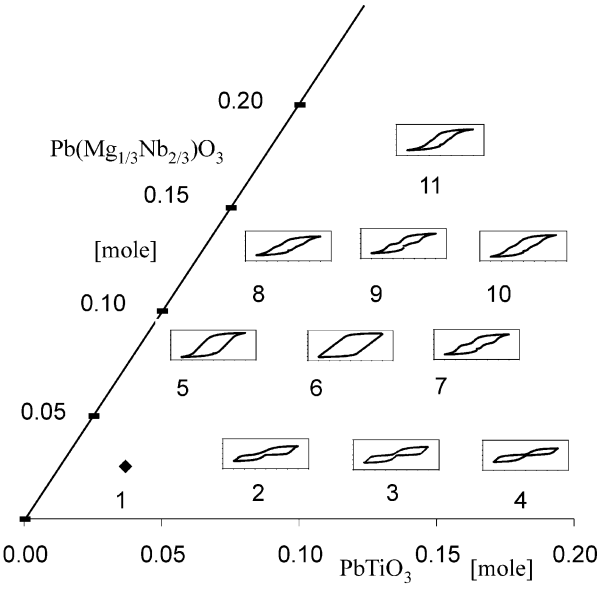

Fig. 13. Ternary diagram showing P–E hysteresis loops (axes scale: $E = \pm 40$ kV/cm, $P = \pm 30$ μC/cm^2).

1, 5 and 8 which only contained ~2.5 mol% of Ti did not show any phase transitions apart from at the Curie point. However as the Ti content is so small, any antiferroelectric–$F_{R(HT)}$ phase transition might be too close to the Curie point to observe from the dielectric data. Where a low temperature phase transition was observed, there is an increase in transition temperature with increasing Ti-content, which parallels a similar trend observed for the $PbZrO_3$–$PbTiO_3$ binary system for Ti-contents in the range ~6–20 mol%. The effect of increasing the MgNb content for any particular composition is shown to reduce the transition temperature towards room temperature.

4.4. Curie point transition properties

The variation in Curie point temperatures across the ternary phase diagram as shown by Fig. 8 shows two discernable trends. As the Ti content increases there is an increase in T_c, which is consistent with the trend known for the $PbZrO_3$–$PbTiO_3$ binary system. In contrast, the T_c is seen to decrease as the MgNb content increases, which again is consistent as $PbMg_{1/3}Nb_{2/3}O_3$ has a much lower Curie point than $PbZrO_3$. The other interesting observation about the Curie point phase transition is that all the compositions appear to show characteristic hysteresis effects between heating and cooling. Fig. 6 shows the dielectric response of composition 6 with temperature, which shows a peak to peak temperature difference of ~9 °C between heating and cooling for the dielectric constant data, and across all compositions this peak to peak temperature difference ranged between 6 and 11 °C. Application of the Curie–Weiss law[25] to these phase transitions in terms of plotting ε^{-1} versus temperature showed good linearity. Table 2 summaries the results of this analysis and includes values taken from the dielectric constant vs. temperature plots. There was little evidence that the transition showed a diffuse nature as is observed in relaxor ferroelectrics such as $Pb(Mg_{1/3}Nb_{2/3})O_3$ itself, and this seems to be the case based on the statistical R-squared values for each plot being unity. The fact that all the calculated Curie–Weiss temperatures were smaller than the Curie point temperatures (as determined from the maxima of the dielectric constant vs. temperature plots) also indicate a first order type phase transition. The calculated Curie–Weiss constants do show an increase with increased Ti-content for a fixed MgNb-content, but are effectively constant for increases in the MgNb-content at a particular Ti-content. The observation of apparent hysteresis at the Curie point was certainly unexpected and there was no evidence to say it might be an artifact of the measurement technique. However, we do not have an explanation for this unusual observation, or why the two maxima peaks of the dielectric constant at T_c are different.

Table 2
Compiled Curie-point data from ε vs. temperature and $1/\varepsilon$ vs. temperature plots

Sample code	R-Squared	Curie-constant ($\times 10^5$ °C)	Curie–Weiss temp (°C)	Transition temp. (heating) (°C)	Transition temp. (cooling) (°C)	ε (heating)	ε (cooling)
1	0.999	2.28	197	229	218	8301	10536
2	0.997	2.83	217	241	230	15822	19308
3	0.997	2.95	242	258	251	17070	18144
4	0.984	4.50	247	279	273	14730	15377
5	0.999	2.31	200	218	211	16500	19520
6	0.996	2.96	205	230	221	14741	16893
7	0.988	4.41	228	254	244	21330	25403
8	0.996	2.31	198	214	206	16205	20442
9	0.991	3.16	207	226	217	20471	25659
10	0.984	4.18	219	242	235	18444	21294
11	0.984	2.99	197	210	203	21054	25596

4.5. Resistivity

The control of the resisitivity for the material in the pyroelectric array is important as it determines how quickly the material readjusts due to changes in the image. In the case of high resistivity materials, the slow time constant associated with the discharge of current would produce slow response time for the array. In contrast, if the resistivity is too low, this can result in electrical breakdown during the poling stage. Fig. 12a shows that the range of resistivities ($0.5–5\times 10^{11}$ Ωm) across the phase diagram was relatively insensitive to the change in composition and showed no discernable trend. Fig. 12b shows the effect of changing the Mn content and the Pb excess based on the Ti and MgNb contents of compositions 6 and 4, respectively. In general, the samples showed resistivity values invariant with the compositional changes.

Direct comparison with the previous PZTMN study[15] where MnO_2 was used as a dopant is difficult, as the composition studied contained much more Ti and MgNb content. However, for similar doping levels, the dielectric loss values are consistently low, which was the prime reason for trying MnO_2. The effect of adding 0.5 wt.% MnO_2 in the previous study produced quite a sharp increase in resistivity, but not much variation for 0.5–1.0 wt.% addition. Previous work[22] had also shown that changing Pb excess could be used to control resistivity in an uranium doped PZT–iron niobate ceramic. What seems to be the case in the present study is that the effect of the MnO_2 addition on the resistivity saturates at relatively low MnO_2 levels but hinders any Pb excess effects. If this is the case, the fact that the effect of adding MnO_2 shifts the resistivity away from the required resistivity range suggests an alternative dopant may be necessary either to replace the MnO_2 or compete with the Mn presence. Also, it is worth noting that in a previous study,[8] where uranium was successfully used as a dopant to control resistivity, the value of the activation energy determined from resistivity versus (temperature)$^{-1}$ studies was $\sim$0.77 eV for U-contents $<$0.4 mol% and $\sim$0.37 eV for greater dopant levels. This was attributed to hole conduction dominating at the lower doping levels and electron conduction dominating at higher levels after Pb-vacancies had been compensated for by the uranium ions acting as donors. The equivalent activation energy determined for composition 6 was found to be 0.57 eV, which may be characteristic of hole conduction in the present system and may account for low resistivity values measured. A subsequent study of the effect of uranium doping levels on the resisitivity of samples based on composition 4 has been carried out and reported.[28]

4.6. P–E hysteresis loops

Fig. 13 summarises the shapes of polarisation-field (P–E) hysteresis loops obtained across the phase diagram. In each case signs of saturation were observed for the 30 kV/cm applied field, and the coercive field strength was found to be between 10 and 20 kV/cm. Compositions 2, 3 and 4 which contain the least amount of MgNb content, show a characteristic double loop phenomena which is more pronounced with increasing Ti content, which shows some consistency with earlier studies[23,24] carried out on undoped PZT. In particular,[24] a composition with 6% Ti content had shown an open hysteresis loop, whereas at 12% Ti content distinct double loop hysteresis was apparent. In the present studies, compositions 2 and 3 most closely resemble the composition of those samples with 7.5 and 12.5% Ti content, respectively, as well as the lowest MgNb content. Although both samples showed considerable amounts of double loop phenomena, composition 2 showed slightly the more expected open loop phenomena and it well may be that the slightly lower Ti content of the comparable sample from the previous work[24] is a crucial factor. Certainly the proximity of the composition to a room temperature phase change (i.e. rhombohedral–tetragonal, or antiferroelectric–rhombohedral), seemed to produce good open hysteresis loops, whereas changing the Ti-content away from the phase boundary into the rhombohedral phase region

within a few percent was enough to produce the double loop behaviour. At greater MgNb concentrations, some of the compositions show slight evidence of this double loop phenomenon, but all maintain a non-zero remnant polarisation value. The other factor to consider in increasing the MgNb content is how the lowering of the $F_{R(HT)}$–$F_{R(LT)}$ phase transition towards room temperature may influence the hysteresis loops. The combination of these competing forces may account for the apparent nonuniform trend in loop shapes at higher MgNb levels. It is interesting to note that although compositions 3 and 4 show the most double loop characteristic, in which the remnant polarisations almost relax to zero at zero field, the pyroelectric coefficients and F_D FOM values indicate that their pyroelectric properties are not adversely affected. Possible microstructural mechanisms for the double loop hysteresis in similar undoped PZT compositions have been discussed elsewhere.[24]

5. Conclusions

The studies carried out in the $Pb(Mg_{1/3}Nb_{2/3})O_3$–$PbTiO_3$–$PbZrO_3$ system have shown that there are viable ceramic compositions, which compare favourably with commercial ceramics in terms of their FOM values. The observation of compositional effects on the $F_{R(HT)}$–$F_{R(LT)}$ phase transition temperature has also meant that compositions can be chosen such that undesirable hysteretic effects from the proximity of first order phase transitions within the working temperature window of the pyroelectric material can be minimalised. The resistivity of the system has also been shown to be fairly invariant to compositional change, which for some applications may be a positive attribute. The use of alternative dopants to vary resistivity within this system is an important area for future investigation.

Acknowledgements

The authors would like to thank the EPSRC (under Project No. GR/L91436) and InfraRed Integrated Systems Limited (Towcester, UK) for the funding of this work. RWW gratefully acknowledges the financial support of the Royal Academy of Engineering.

References

1. Whatmore, R. W. and Watton, R., Pyroelectric ceramics and thin films for uncooled thermal imaging. *Ferroelectrics*, 2000, **236**, 259–279.
2. Watton, R., *Ferroelectrics*, 1976, **10**, 91.
3. Liu, S. T. and Long, D., *Proc. IEEE.*, 1976, **66**, 14.
4. Porter, S. G., *Ferroelectrics*, 1981, **33**, 193.
5. Whatmore, R. W., Pyroelectric materials and devices. *Reports on Progress in Physics*, 1986, **49**, 1335–1386.
6. Ichinose, N., *Am. Ceram. Soc. Bull.*, 1985, **64**, 1581.
7. Kobune, M., Fujii, S. and Asada, K., *J. Ceram. Soc. Japan*, 1984, **104**(4), 259–263.
8. Whatmore, R. W. and Ainger, F. W., *Proc. SPIE*, 1983, **395**, 261.
9. Whatmore, R. W. and Bell, A. J., *Ferroelectrics*, 1981, **35**, 155.
10. Whatmore, R. W., High performance conducting pyroelectric ceramics. *Ferroelectrics*, 1983, **49**, 201–210.
11. Clarke, R., Glazer, A. M., Ainger, F. W., Appleby, D., Poole, N. J. and Porter, S. G., Phase transitions in lead zirconate titanate and their applications in thermal detectors. *Ferroelectrics*, 1976, **11**, 359–364.
12. Adachi, M., Hachisuka, A., Okumura, N., Shiosaki, T. and Kawabata, A., Pyroelectric and dielectric properties of rhombohedral $Pb(Zr_{1-x}Ti_x)O3$ ceramics. *Japan. J. Appl. Phys. Supplement*, 1987, **26–2**, 68–71.
13. Whatmore, R. W., Shorrocks, N. M., Osbond, P. C., Stringfellow, S. B., Carter, C. F. and Watton, R., Modified lead scandium tantalate for uncooled LWIR detection and thermal imaging. *In Proc. 8th International Symposium on the Applications of Ferroelectrics, Greenville, SC, September* 1992, pp. 202–205. IEEE Cat. No. 92CH 3080–9.
14. Ouchi, H., Nagano, K. and Hayakawa, S., *J. Am. Ceram. Soc.*, 1965, **48**(12), 630–635.
15. Ouchi, H., Nishida, M. and Hayakawa, S., *J. Am. Ceram. Soc.*, 1966, **49**(11), 577–582.
16. Ouchi, H., *J. Am. Ceram. Soc.*, 1968, **51**(3), 169–176.
17. Navarro, A., Shaw, C. P., Alcock, J. R. and Whatmore, R. W., A Taguchi study of defects in the fabrication of P. Z. T. Ceramics. In *Workshop Proceedings of Ferroelectrics 2000 UK (IOM Cummunications)*, 2000, pp. 29–36.
18. Choi, S. W., Jang, S. J. and Bhalla, A., *J. Korean Physical Society*, 1989, **22**(1), 91–96.
19. Swartz, S. L. and Shrout, T. R., Fabrication of perovskite lead magnesium niobate. *Mater. Res. Bull.*, 1982, **17**, 1245–1250.
20. Butcher, S. J. and Daglish, M., The use of magnesium carbonate hydroxide pentahydrate in the production of perovskite lead magnesium niobate. In *Proc. Third Euro-Ceramics*, Vol. 2, ed. P. Duran and J. F. Fernandez. Pub. Faenza Editrice Iberica S.L., 1993, pp. 121–126.
21. Byer, R. L. and Roundy, C. B., *Ferroelectrics*, 1972, **3**, 333.
22. Bell, A. J. and Whatmore, R. W., Electrical conductivity in uranium doped, modified lead zirconate pyroelectric ceramics. *Ferroelectrics*, 1981, **37**, 543–546.
23. Dai, X., Xu, Z. and Viehland, D., *J. Am. Ceram. Soc.*, 1995, **78**, 2815–2827.
24. Ricote, J., Whatmore, R. W. and Barber, D. J., *J. Phys: Condens. Matter*, 2000, **12**, 323–337.
25. Xu, Y. *Ferroelectric Materials and Their Applications*. North-Holland, Amsterdam, 1991, pp. 12–14.
26. Whatmore, R. W., *Ferroelectric Ceramics*. UK Patent 9904027, 1999.
27. Whatmore, R. W., *Rep. Prog. Phys.*, 1986, **49**, 1335.
28. Stringfellow, S. B., Gupta, S., Shaw, C., Alcock, J. R. and Whatmore, R. W., Electrical conductivity control in uranium-doped $PbZrO_3$–$PbTiO_3$–$Pb(Mg_{1/3}Nb_{2/3})O_3$ pyroelectric ceramics. *J. Eur. Ceram. Soc.*, 2002, **22**(4), 573–578.